Oxygen vacancy effects on polarization switching of ferroelectric Bi_2FeCrO_6 thin films

X. Henning,[1] K. Alhada-Lahbabi,[2] D. Deleruyelle,[2] B. Gautier,[2] L. Schlur,[1]
T. Fix,[3] S. Colis,[1] A. Dinia,[1] and M. V. Rastei[1,*]

[1]*Institut de Physique et Chimie des Matériaux de Strasbourg, CNRS, Université de Strasbourg, 23 rue du Loess, F-67034 Strasbourg, France*

[2]*Université Lyon, INSA Lyon, CNRS, Ecole Centrale de Lyon, Université Claude Bernard Lyon 1, CPE Lyon, INL, UMR5270, 69621 Villeurbanne, France*

[3]*ICube Laboratory, CNRS and Université de Strasbourg, 23 rue du Loess, 67037 Strasbourg, France*

(Received 11 January 2024; accepted 26 April 2024; published 21 May 2024)

The controlled switching of spontaneous polarization in ferroelectrics by applying an external electric field is essential for many device operations. Oxygen vacancy defects commonly found in oxide ferroelectrics offer a tempting means for polarization switching regulation at an atomic scale. This study presents a method involving a series of annealing cycles under various environments to modulate the amount of oxygen vacancies in ferroelectric Bi_2FeCrO_6 thin films. By performing a piezoresponse force microscopy study after each annealing cycle, it is shown that a high content of oxygen vacancies induces specific fingerprints on polarization hysteresis loops. Reducing oxygen vacancy density by annealing in oxygen-rich environments results in hysteresis loops being wider and displaying less imprint, while increasing oxygen vacancy density by annealing in oxygen-poor environments results in thinner and more imprinted hysteresis loops. The process is largely reversible, constituting an alternative method for polarization switching control at specific electric fields. Ferroelectric phase-field calculations and energy level diagrams obtained through ellipsometry, Kelvin probe, and photoemission spectroscopy indicate a combined switching mechanism based on a doping effect due to oxygen vacancies and a built-in electric field originating from the interface. Our study is helpful for designing ferroelectric films with a precise imprint or, more generally, for understanding the impact of charged defects on the polarization states in ferroelectric films.

DOI: 10.1103/PhysRevMaterials.8.054416

I. INTRODUCTION

Oxygen vacancies (V_O) are one of the most encountered atomic-scale defects in perovskite oxide thin films. They are either neutral, V_O^0, or positively charged, V_O^{1+} and V_O^{2+}, generating doping and structural relaxation effects [1–5]. Oxygen vacancies can also lead to local strain variations [6,7], discrete in-gap levels [8], photoactive and resistive states [9,10], or to changes of polarization states through various mechanisms [11–14]. In general, the effects induced by oxygen vacancies in ferroelectrics are still not fully understood, motivating, for instance, research of oxygen-free materials [15,16].

Nevertheless, since the discovery of the bulk photovoltaic effect in ferroelectrics [17–19], several oxide ferroelectric-based solar cell devices have been designed [4,19–23], reaching, at most, a power conversion efficiency of 8.1% in the case of Bi_2FeCrO_6 (BFCO) thin films [24]. However, many photovoltaic mechanisms have been reported for BFCO [3,4,21–27], making it a complex physical system where it is still challenging to understand the role of structural defects [28,29]. As oxygen vacancies are expected to modify the ferroelectric properties [30,31], it is therefore important to consider their role in the polarization response of BFCO films to electric fields.

In fact, oxygen vacancies are known to induce voltage offsets and imprint in $(Pb,La)(Zr,Ti)O_3$ thin films capacitors [14,32]. A recent study realized on a $Pb(Zn_{1/3}\ Nb_{2/3})O_3 - 4.5\%\ PbTiO_3$ bulk single crystal shows, for instance, a large imprint reduction after annealing under an oxidizing atmosphere, an effect attributed to a decrease of oxygen vacancy density [13]. More recently, oxygen vacancies were also found to be critical for controlling the imprint in HfO_2-based ferroelectric capacitors [33,34]. For $BiFeO_3$ thin films, oxygen vacancies were identified to interfere with the polarization state by mechanisms involving defect accumulation near the electrodes [35–38], screening, and local strain fields [7,39–41]. In $BaTiO_3$ films, the formation of oxygen vacancies was shown to enhance in the presence of in-plane compressive strain [12]. For $BaTiO_3$, oxygen vacancies were also correlated with the presence of other dopants [42], with a tendency for *p*-type dopants to favor the formation of oxygen vacancies [43]. Even if a link with imprinting phenomena was not investigated in each of these previous studies, they clearly demonstrate a strong relationship between the ferroelectric polarization state and oxygen vacancy content.

Here, we report effects induced by different concentrations of oxygen vacancies on the polarization reversal of ferroelectric BFCO thin films. This is realized by means of thermal treatments under oxidizing and reducing conditions and various temperatures. With respect to previous studies, it is shown that oxygen vacancies influence the polarization switching

*Corresponding author: mircea.rastei@ipcms.unistra.fr

through a combined mechanism involving a shift (resulting from an interfacial built-in electric field) and a constrictive effect (resulting from oxygen vacancy doping). By analyzing the polarization switching characteristics as a function of thermal treatments and environmental conditions, a significant degree of reversibility in injecting/extracting the oxygen vacancies from the films is also demonstrated. The study includes an advanced statistical analysis of a large number of locally acquired ferroelectric hysteresis loops performed by piezoresponse force microscopy (PFM) at similar locations (nanometer-scale resolution) after each annealing cycle. Strict experimental conditions ensured no effects related to modifications of sample morphology due to annealing time, annealing temperatures, or applications of high voltages. The experimental results are confronted with ferroelectric phase-field calculations able to study the effect of built-in electric fields and doping effects induced by oxygen vacancies on polarization reversal. The role played by the energy level distribution at the interface with the substrate is also discussed.

II. EXPERIMENTAL DETAILS

A. Sample growth and characterization

BFCO thin films were grown by pulsed laser deposition (PLD) on Nb (0.7 at%)-doped $SrTiO_3$(001) (Nb:STO) substrates (Codex International). The film was obtained by ablating a homemade ceramic target. The base pressure in the growth chamber prior to deposition was 5×10^{-8} mbar. The growth was made with an oxygen partial pressure of 10^{-2} mbar at a substrate temperature of 740 °C. A KrF excimer laser with a 248 nm wavelength was used. The laser modulation and fluence were 5 Hz and 3 J/cm^2, respectively. The PLD is equipped with a reflection high-energy electron diffraction (RHEED) technique which allows one to determine the crystallinity and the surface arrangement of the thin film at the end of its growth.

The crystalline structure of the film was analyzed by x-ray diffraction using a Rigaku Smartlab diffractometer with a rotating anode and a monochromatic copper source (45 kV, 200 mA, 0.154056 nm). X-ray diffraction (XRD), x-ray reflectivity (XRR), and reciprocal space mapping (RSM) measurements were performed. To determine the sample thickness (62 nm), XRR curves were fitted with the Rigaku-Globalfit software.

Atomic force microscopy (AFM) measurements were performed with a Bruker Dimension Icon microscope. The local ferroelectricity, including measurements of the hysteresis loops, was investigated by standard piezoresponse force microscopy (PFM). The probe was a 0.01–0.025 Ω cm antimony (n) doped Si covered with conductive diamond. A cantilever with a stiffness of about 80 N m^{-1} was used. The used set point was about 800 nN. For writing up and down domains and for the acquisition of hysteresis loops, an additional DC voltage was applied to the tip. Hysteresis loops were recorded at a rate of 0.1 Hz by ramping the tip bias voltage from −6 to 6 V and then back to −6 V. In this bias interval, no correlation between the small current-voltage values and the piezo-response (PR) quadrature signal has been detected. Hysteresis loops and piezoresponse (PR) mapping were acquired using a $V_{AC} = 2$ V applied to the substrate, at a frequency of 45 kHz, and with a drive phase set at +50° to maximize the PR quadrature signal and hence minimize the PR in-phase signal. Up and down domains were written by applying a tip bias of −6 and 6 V, respectively.

TABLE I. Parameters of annealing cycles. Heating and cooling ramps of an annealing cycle were performed in about one hour and a half for dry air conditions. In the case of annealing under H_2/Ar conditions, 4 hours of heating and 6 hours of cooling were required.

Annealing conditions			
Label	Gas composition	Flux (sccm)	Pressure (atm)
Dry air	20% O_2; 80% N_2	150	1
H_2/Ar	5% H_2; 95% Ar	150	1
Annealing steps			
Chronology	Conditions	Temperature (°C)	Time (h)
No. 1	Dry air	350	2
No. 2	H_2/Ar	350	2
No. 3	H_2/Ar	450	2
No. 4	Dry air	450	4
No. 5	H_2/Ar	450	4

B. Methodology and protocols

As shown in Table I, five annealing cycles, labeled chronologically from nos. 1 to 5, were performed. Dry air or H_2/Ar gas atmosphere were used in order to decrease or increase the density of the oxygen vacancies, respectively [13,44–47]. To check the reversibility of the imprint and investigate its dependency on oxygen vacancy concentration, an annealing protocol involving a specific order was adopted. Namely, the amount of oxygen vacancies was decreased during annealing cycles 1 and 4, and increased during cycles 2, 3, and 5. Annealing cycles 2 and 3 were performed under the same gas conditions but at different temperatures. At annealing cycles 4 and 5, the sample was annealed two times longer than it was during the previous cycles to verify if saturation effects can be reached. Annealing cycle 0 corresponds to the initial state, i.e., the as-prepared state. At each annealing cycle, including 0, 100 PR hysteresis loops were acquired, except for cycle 4 where 35 hysteresis loops were recorded.

III. RESULTS AND DISCUSSION

A. Imprint and PR quadrature signal

Surface topography and PFM signals measured before annealing cycle 1 (initial state) are shown in Fig. 1. The topography shows surface height variations of a few nanometers [Figs. 1(a) and 1(d)]. Before imaging, two 3×3 μm^2 zones were poled up and down, respectively, by applying −6 and 6 V DC bias to the AFM tip. Those zones appear, respectively, as bright and dark areas in the PFM phase imaging [Fig. 1(b)]. The other two unpoled 3×3 μm^2 zones correspond to the as-grown state of the sample, i.e., zones that were never poled. They do not exhibit a uniform out-of-plane PR phase signal. A nearly 180° phase difference between up-poled and down-poled zones can be observed [Fig. 1(e)]. This is consistent

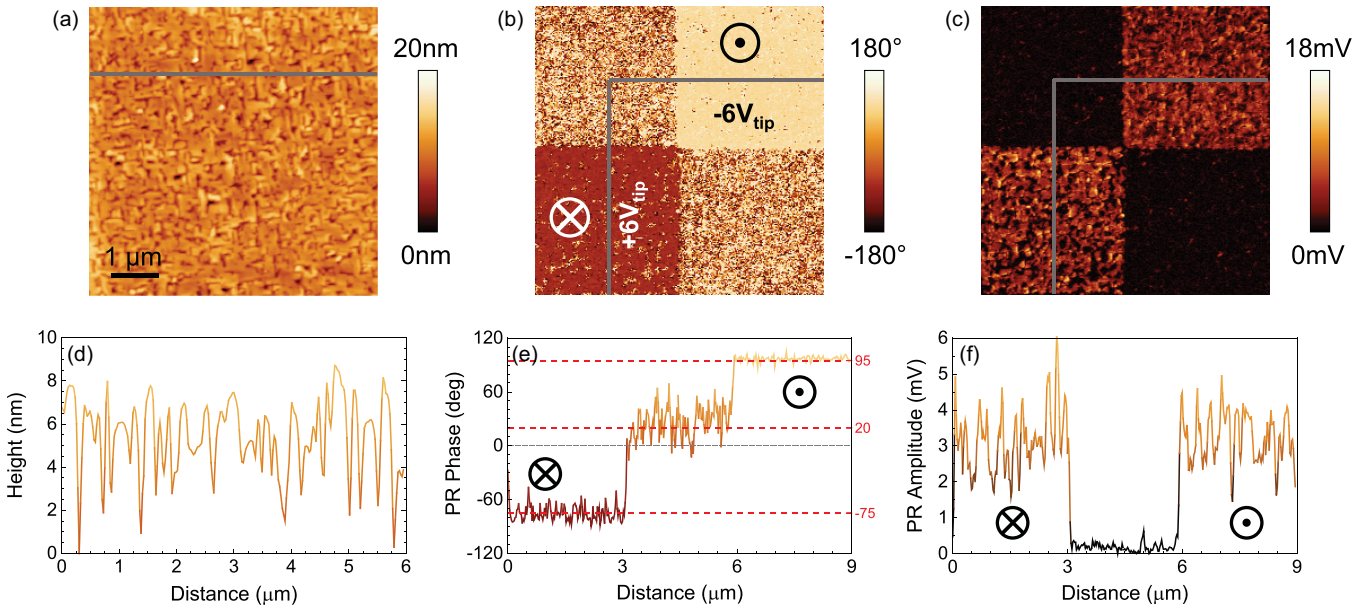

FIG. 1. (a) $6 \times 6\ \mu m^2$ AFM topography of BFCO surface taken before annealing cycle no. 1, i.e., the initial state. Gray line is the location of the profile from (d). (b) Out-of-plane piezoresponse phase image of the area from (a) acquired after poling upward (bright contrast) and downward (dark contrast) the two zones labeled $-6V_{tip}$ (dot circled symbol) and $+6V_{tip}$ (cross circled symbol), respectively. Gray line is the location of the profile from (e). (c) Out-of-plane piezoresponse amplitude image acquired simultaneously with images (a) and (b). Gray line is the location of the profile from (f). (d)–(f) are profiles acquired along the gray lines from (a)–(c), respectively.

with the PR amplitude image [Fig. 1(c)], where a similar amplitude (≈3 mV) on both up- and down-poled zones is measured, as expected from ferroelectric domains with opposite orientation. A weaker PR amplitude signal in the two unpoled zones is observed. This is related to the fact that one coercive field falls near zero-bias voltage for the initial state, an effect induced by the imprint.

PR signals were also acquired by maintaining the tip in contact with the film surface at fixed locations, i.e., center of grains imaged in topography. To derive imprint values from such PR signals, the method proposed by Jesse *et al.* [48] was used. It consists in fitting the quadrature signal [Fig. 2(a)] with a sigmoid function,

$$Y^{\pm}_{\text{piezo}}(V) = a_1 - a_2\left[1 + \exp\left(\frac{V - a_3^{\pm}}{a_4}\right)\right]^{-1} + Va_5, \quad (1)$$

where V stands, in this case, for DC bias applied to the AFM tip. Parameters a_x, with $x = 1, 2, \ldots$, describe the switching characteristics of the loops [48]. The coercive fields are captured by a_3^+ and a_3^-, revealing the switching bias values V^+ and V^- of the forward and backward branches of the loops, respectively. The imprint value is thus given by

$$\left.\frac{d^2 Y_{\text{piezo}}(V)}{dV^2}\right|_{V=V^{\pm}} = 0 \Leftrightarrow V^{\pm} = a_3^{\pm} \quad (2)$$

and

$$\text{Imprint} = \frac{a_3^+ + a_3^-}{2}. \quad (3)$$

Sigmoid fits were performed on PR quadrature signals rather than phase signals because the latter is more subject to artifacts such as piezoelectric amplitude offsets arising from electrostatic interactions. Indeed, the phase signal can be very different from one measurement to another, while the quadrature signal is more consistent (see Figs. S1 and S2 in the Supplemental Material [49]). The drive phase was set during the measurements in such a way that the quadrature signal is maximized and the in-phase signal minimized [Figs. 2(a) and 2(b)]. The analysis of the quadrature hysteresis loops is necessary in our case because, as seen in Fig. 2(a), the PR quadrature signal is not symmetric with respect to the zero value of the y axis. This causes an asymmetry in the PR amplitude signals as well [Fig. 2(d)], as smaller values are measured for a negative tip bias (up polarization), i.e., the direction of imprint [Fig. 2(a)]. It is thus possible that the imprint not only shifts the coercive fields, but also modifies the amplitude response. In turn, the fact that the PR quadrature signal is rather flat when crossing the zero value of the y axis explains the noise enhancement and the fluctuating coercive field values in the phase channel (see Fig. S2 in the Supplemental Material [49] for details). Note that phase and quadrature signals would give equivalent coercive fields if the quadrature signal sharply crosses the zero value of the y axis, i.e., a more symmetric loop with respect to the zero value of the y axis, as usually observed for most ferroelectric thin films.

B. Annealing effects

Hysteresis loops corresponding to the initial state (as-grown state) of the sample are shown in Fig. 2. A significant imprint can be observed, which consists in a lateral shift of the center of the PR quadrature loop along the applied voltage (x axis). In Fig. 2(a), this is shown by a dashed vertical line. The two branches of the loop in Fig. 2(a) were fitted using the sigmoid function from Eq. (1), leading to an evaluation of

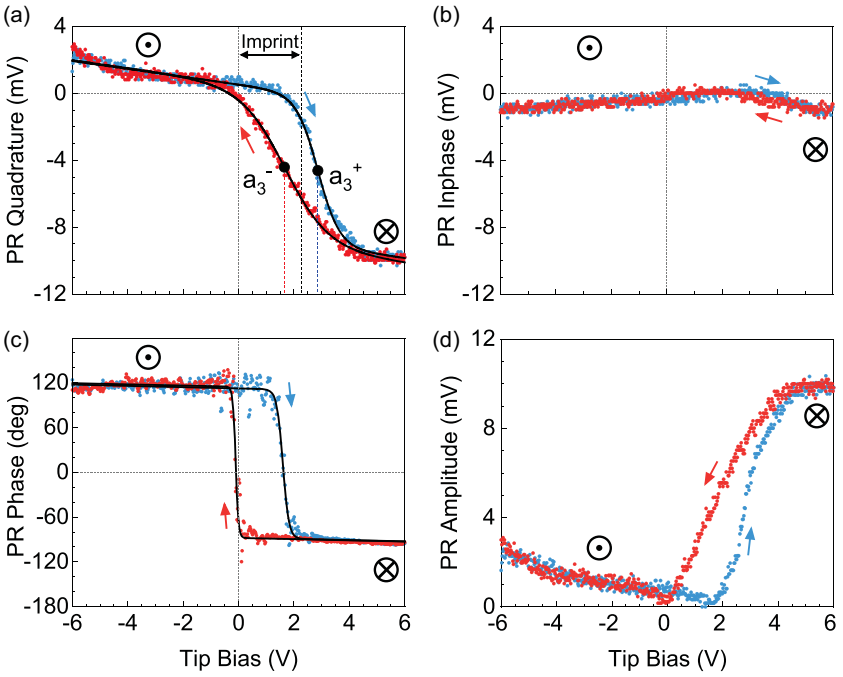

FIG. 2. (a) Quadrature, (b) in-phase, (c) phase, and (d) amplitude components of a piezoresponse (PR) signal. Solid black lines in (a) are sigmoid fits following Eq. (1). Black dots are a_3^+ and a_3^- values extracted from the fits of forward and backward branches of the loops. The imprint [double end arrow in (a)] is 2.27 V in this case (sample in its initial state). Thick lines in (c) are smooth lines through the phase signal.

the a_3^+ and a_3^- values, and thus to the imprint using Eqs. (2) and (3).

Typical hysteresis loops acquired with the sample in (i) its initial state, (ii) after annealing under dry air (annealing cycle 4), and (iii) after annealing under H_2/Ar (annealing cycle 5) are compared in Fig. 3. As seen, the loop measured after annealing under dry air looks very different with respect to the loop measured for the initial state [Fig. 3(a)], indicating that V_O vacancies largely influence the polarization switching fields. In turn, the loop measured after annealing under H_2/Ar is similar to the one obtained for the initial state [Fig. 3(b)]. This suggests that the sample contains oxygen vacancies in its initial state. A statistical analysis of all hysteresis loops acquired after each annealing cycle was performed following the procedure described in Sec. III A.

C. Switching-field and imprint distribution

The mean and standard deviation values of the $a_3^\pm$ switching parameters as well as of the imprint are presented in Table II. An example of how those parameters are obtained is shown in Fig. 4(a) for the initial state of the sample. The dashed line is a normal distribution fit of the data, which reveals the mean and standard deviation values of the imprint. A similar fit was carried out for each data set obtained after each annealing cycle. The normalized distribution functions are gathered in Fig. 4(b). Notably, it can be observed that the imprint can be reversibly tuned to lower or higher values depending on annealing conditions. Annealing cycles 1 and 2 correspond to an annealing temperature of 350 °C and an annealing time of 2 hours. The variations of the imprint values thus seem to mainly be induced by the gas nature used during the annealing. A similar conclusion can be drawn after analyzing the effects induced by annealing cycles 4 and 5, both corresponding to 450 °C and an annealing time of 4 hours.

Again, these results point out that the initial state of the sample already contains a significant amount of oxygen vacancies. By increasing the annealing time and temperature, oxygen vacancies are further removed or introduced as compared to previous annealing cycles under dry air or H_2/Ar conditions, respectively. However, it was impossible in this study to decrease the imprint down to zero through annealing treatments only. The lowest imprint value of about 1.2 V obtained after annealing cycle 4—where the V_O density should be the lowest—suggests the existence of an additional electric field not related to oxygen vacancies. Note that on other samples, we found that using higher temperatures may induce morphological modifications of the sample.

It is also worth noticing that the mean uncertainty $\langle\delta\rangle$ values of the imprint are always smaller than the standard deviation values, indicating that the measured imprint distribution does not result from a lack of accuracy (Table II). Uncertainty on imprint values is higher after annealing cycles in dry air, as seen for cycles 1 and 4. This is due to a reduced PR response and a more complex loop shape which imposes sigmoid fits over a slightly truncated bias range to allow a

TABLE II. Statistical results obtained by analysis the PR quadrature hysteresis loops measured on the same sample after each annealing cycle. Forward and backward switching voltage values, respectively, a_3^+ and a_3^-, are extracted following the fitting procedure described in the main text. Imprint values are deduced from $a_3^\pm$ parameters according to Eq. (3). Results follow the format "mean value ± standard deviation value." $\langle\delta\rangle$ and I_C at 2σ are the mean uncertainty on the imprint value and the confidence interval of the mean imprint value, respectively.

	No. 0 (Initial state)	Annealing no. 1 (Dry air)	Annealing no. 2 (H_2/Ar)	Annealing no. 3 (H_2/Ar)	Annealing no. 4 (Dry air)	Annealing no. 5 (H_2/Ar)
a_3^+ (V)	2.58 ± 0.25	2.77 ± 0.39	3.06 ± 0.39	3.15 ± 0.29	3.55 ± 0.85	3.15 ± 0.42
a_3^- (V)	1.30 ± 0.33	0.15 ± 0.60	0.55 ± 0.48	0.99 ± 0.48	−1.00 ± 0.72	1.09 ± 0.44
Imprint (V)	1.94 ± 0.27	1.46 ± 0.41	1.81 ± 0.33	2.07 ± 0.29	1.28 ± 0.44	2.12 ± 0.26
$\langle\delta\rangle$ (V)	± 0.03	± 0.22	± 0.15	± 0.12	± 0.33	± 0.16
I_C at 2σ (V)	[1.89; 1.99]	[1.38; 1.54]	[1.74; 1.88]	[2.01; 2.13]	[1.13; 1.43]	[2.07; 2.17]

good convergence. The confidence interval of the imprint values at 2σ underlines the significance of the results obtained after each annealing cycle. Overall, as there is no overlap between the confidence intervals obtained after annealing in dry air and those obtained after annealing in H_2/Ar, it can be concluded that the change of imprint value induced by the gas is indeed significant.

Another interesting observation concerns the values of $a_3^\pm$ switching fields (Table II), which indicate that after annealing cycles 3 to 5, the mean imprint values vary almost exclusively because of a change of the left branch of the loops, i.e., a_3^- values. Therefore, the switching of the polarization direction from up to down (towards the interface) does not depend much on the annealing processes, while the switching from down to up does. Understanding how a change of the oxygen vacancy density could lead to such an asymmetry is not straightforward. Nevertheless, the explanation shall comprise an asymmetric potential perpendicular to the film. In the case of a $PbZr_2Ti_{0.8}O_3$ (PZT) film, Han *et al.* suggested that charged oxygen vacancies can preferentially localize at the film surface, hence being a source of asymmetry [2]. Lee *et al.* also have associated the ferroelectric imprint observed in a PZT sample to the presence of oxygen vacancies at the sample surface [50]. Simulations including an asymmetric distribution of oxygen vacancies indeed indicated imprinted hysteresis loops [51].

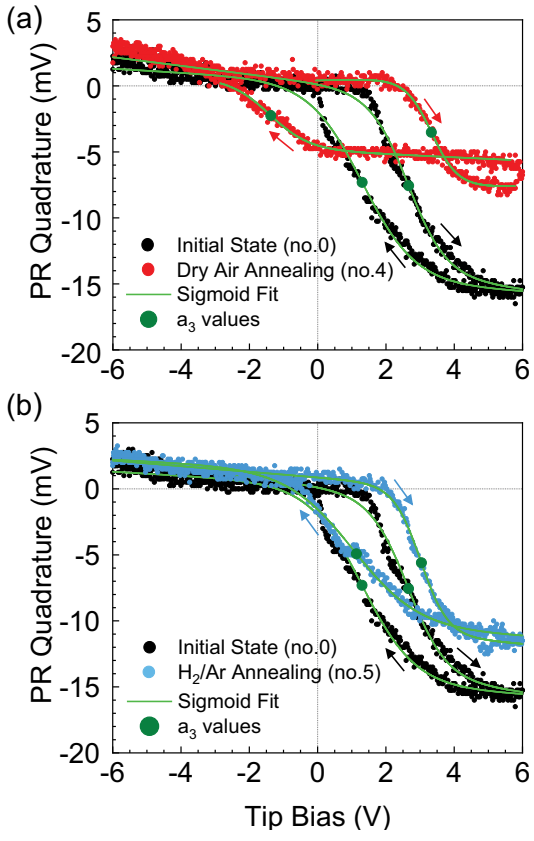

FIG. 3. (a) Hysteresis loop (red) measured after annealing under dry air (annealing no. 4). (b) Hysteresis loop (blue) measured after annealing under H_2/Ar (annealing no. 5). The hysteresis loop measured before annealing the sample (i.e., initial state) is shown in both (a) and (b) for comparison (black data points). Green dashed lines are sigmoid fits, highlighting the $a_3^\pm$ values (green dots).

D. Energy levels at the interface

In addition to the asymmetric change of $a_3^\pm$ switching values, the imprint could arise from an electric field oriented perpendicularly to the film plane. Although such a field may have different origins, its direction must agree with the imprint sign. As discussed above, possible origins for the shift effect can be a nonuniform doping through the sample thickness [51], but any other electric field oriented perpendicularly to the film would generate a similar effect. For instance, interface built-in fields existing within a space charge region generated by the alignment of Fermi levels can induce such a shift. Oxygen vacancies can eventually localize at the film surface [2,50], but this would result in a negative imprint value due to their positive charge, i.e., a loop shifted to the left with respect to 0 V, which is opposite to our observations. Therefore, an interface electric field oriented perpendicularly to the film plane is a plausible explanation for the observed lateral hysteresis loop shift [Fig. 5(a)], as also reported for PZT films [2]. On the other hand, the width of a hysteresis loop can shrink (constrictive effect) by an amount which depends on the V_O doping level [51], as schematically shown in Fig. 5(b). A combined action of constrictive and shift effect can indeed lead to a significant variation of only one of the switching fields, i.e., a_3^- values [Fig. 5(c)], as experimentally observed (Table II).

To gain insights into energy levels of the BFCO/Nb:STO system and check for a possible built-in field at the interface, an advanced photon spectroscopy study, combined with Kelvin probe and ellipsometry measurements, was

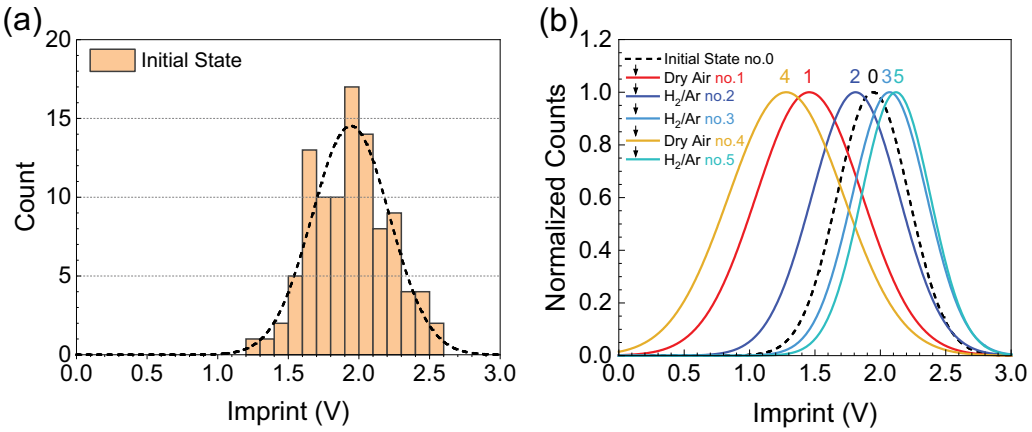

FIG. 4. (a) Distribution of imprint values obtained from 100 hysteresis loops acquired for the initial state. Black dashed curve is a normal distribution fit. (b) Normalized distribution fits of imprint values obtained after each annealing cycle. Inset: The chronology of annealing cycles and annealing conditions (also see Table I).

performed. The results are shown in Fig. 6, which includes a Tauc [Fig. 6(a)] and a photocurrent [Fig. 6(b)] plot (also see Fig. S3 in the Supplemental Material [49]). These results allow one to construct the energy level diagram of the system [Fig. 6(c)], along with the electronic band structure at the interface [Fig. 6(d)]. The *p*-type doping of the BFCO is most likely given by cationic vacancies formed during the deposition, as they were indeed found to be efficient acceptors in BFO films [52]. A Schottky-like contact is thus predicted at the interface with the Nb:STO substrate, which includes a space charge region in the BFCO and the associated built-in electric field. Importantly, as illustrated in Fig. 6(d), the direction of the predicted built-in field is pointing from the interface towards the surface of the film, in consonance with the observed shift of the hysteresis loops and the imprint direction. In addition, note that a downward band bending suggests the presence of negative charges in the depletion region. This can make our films more able to stabilize positively charged oxygen vacancies. To globally address the impact of oxygen vacancy concentration on the polarization switching, simulations based on a ferroelectric phase-field model were carried out.

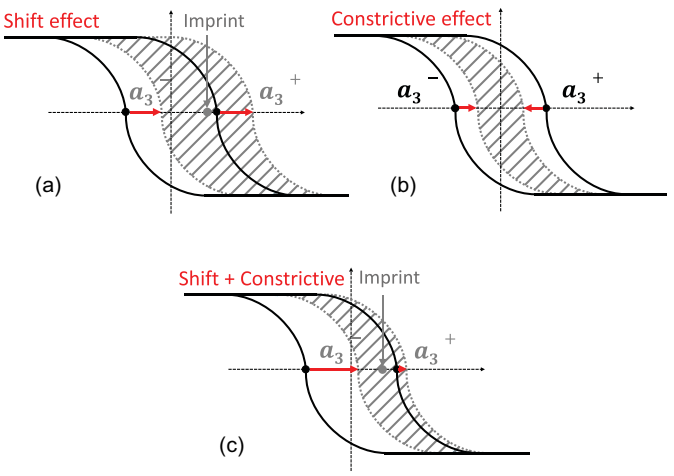

FIG. 5. Schematics of the polarization hysteresis loop modified by (a) a shift effect arising from a built-in electric field, (b) a constrictive effect arising from doping, and (c) both effects combined. Solid black lines represent a hysteresis loop in the absence of the shift and constrictive effects.

IV. PHASE-FIELD SIMULATIONS

The phase-field simulations were conducted using a methodology outlined in previous works [53,54]. The microstructure evolution of the ferroelectric polarization was obtained by the time-dependent Ginzburg-Landau (TDGL)

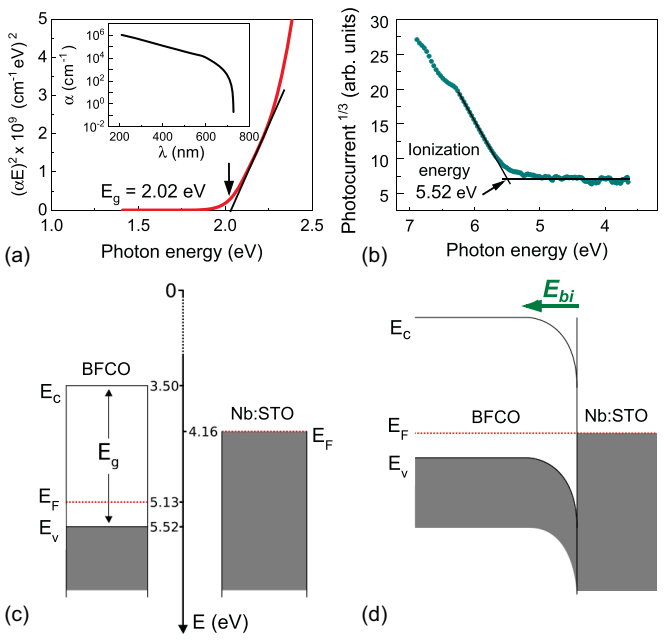

FIG. 6. (a) Tauc plot for a BFCO film grown on a Nb:STO substrate. Inset: The absorption coefficient vs wavelength as obtained from ellipsometry measurements (see Fig. S3 in the Supplemental Material [49]). (b) Photocurrent plot, obtained by photoemission spectroscopy, used to determine the ionization energy. (c) Energy level diagram of the BFCO/Nb:STO structure based on results from (a) and (b). Expected electronic band structure of BFCO/Nb:STO interface. A built-in electric field (E_{bi}) pointing from the Nb:STO towards the BFCO is expected within the space charge region.

equation [55,56],

$$\frac{\partial P_i(\mathbf{r},\mathbf{t})}{\partial t} = -L\frac{\delta\psi}{\delta P_i(\mathbf{r},\mathbf{t})}, \quad (i=1,2), \tag{4}$$

where $P_i(\mathbf{r},t)$ denotes the components of the spontaneous polarization $\mathbf{P}=(P_1,P_2)$, L is a kinetic coefficient, ψ is the total free energy, and $\mathbf{r}=(x,z)$ denotes the spatial vector in two dimensions. Here, $\mathbf{x}$ and $\mathbf{z}$ denote the horizontal and vertical axes, respectively. The vertical z axis was oriented in the downward direction. In this paper, we adopted a simplified model that solely takes into account the polarization with an out-of-plane component, represented as $\mathbf{P}=(0,P_z)$.

The total free energy ψ is given by [55,56]

$$\psi = \int_V (\psi_{\text{bulk}} + \psi_{\text{grad}} + \psi_{\text{elec}})\delta V, \tag{5}$$

in which ψ_{bulk}, ψ_{grad}, and ψ_{elec} are the bulk, gradient, and electric free energy density, respectively. For a direct analysis of the role of the electric charge profile on ferroelectric hysteresis, we excluded the consideration of an elastic free energy term in this study. An example of implementing this energy, along with the relevant boundary conditions for thin films that incorporate the intricacies of the film/substrate interface, can be found in a previous phase-field work [57]. Due to the unavailability of thermodynamic Landau coefficients for Bi_2FeCrO_6, we opted to model a $PbTiO_3$ thin film [58,59], as our main objective was not to quantify the imprint values, but rather to offer a qualitative understanding of how the behavior induced by charge profiles and a built-in electric field affect the hysteresis loops. The simulations were conducted on a discretized $100\Delta x \times 64\Delta z$ two-dimensional grid, where the grid spacing was set to $\Delta x = \Delta z = 1$ nm. More information on the material parameters and free energy computation is provided in the Supplemental Material [49].

The presence of a uniform charge distribution within the film was incorporated following the expression

$$\rho(x,z) = +2qN, \tag{6}$$

where ρ is the charge induced by the doping distribution, $q = 1.6\times10^{-19}$ C is the elementary charge, and N is the doping concentration. In our simulations, we considered a positively charged doping profile. In addition, simulations were also carried out while directly incorporating an additional built-in electric field. In these cases, the presence of an internal field $E_z^{\pm}$ originating from the bottom electrode was modeled as

$$E_z^{\pm}(x,z) = \begin{cases} E^{\pm}\left(1-\frac{z}{\tau}\right) & \text{if } z<\tau \\ 0 & \text{if } z \geqslant \tau, \end{cases} \tag{7}$$

where $E^{\pm} = \pm E_0$, with E_0 is the electric field amplitude, depending on whether the field is oriented upward or downward, and τ is a critical thickness above which the field totally vanishes in the layer. Examples of such profiles are provided in Fig. S4 in the Supplemental Material [49]. Ferroelectric hysteresis loops were obtained by applying a voltage ramp to the top electrode, as experimentally the voltage was applied to the tip. An electric field ranging from -5 to 5 MV/cm within the layer was considered. To solve the electrostatic equilibrium, we employ the spectral method [60–62]. For further information on how the voltage was applied in the simulations, please refer to the Supplemental Material [49]. To investigate in detail the ferroelectric hysteresis behavior in the presence of charges and an internal built-in electric field, a series of simulations was conducted. First, we examined the response to a uniform charge profile within the layer in a range of doping concentrations from $N = 1\times10^{19}$ cm^{-3} to $N = 2\times10^{20}$ cm^{-3}. As seen in Fig. 7, the hysteresis loop symmetrically contracts until it becomes completely linear above a concentration of $N = 2\times10^{20}$ cm^{-3}, a physical trend aligning with the previous literature [51,63]. This is the effect of doping-induced charge which surpasses the polarization charge at high concentration values.

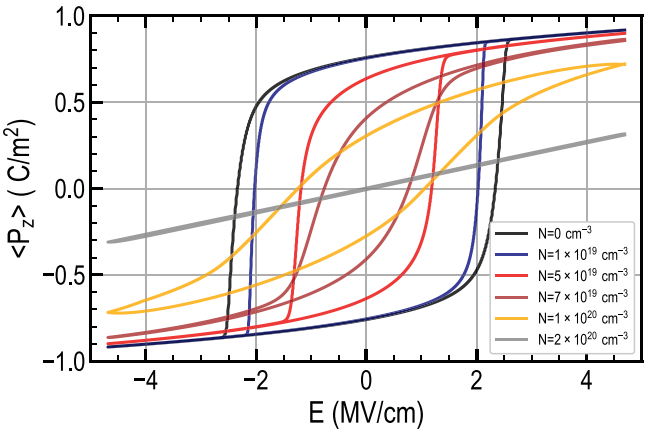

FIG. 7. Ferroelectric hysteresis loops obtained by phase-field simulations. A uniform dopant distribution across the ferroelectric film is considered. Different hysteresis loops correspond to different dopant concentrations ranging from $N = 1\times10^{19}$ cm^{-3} to $N = 2\times10^{20}$ cm^{-3}.

Subsequently, we investigated ferroelectric hysteresis scenarios involving upward-oriented and downward-oriented built-in electric fields $E_z^{\pm}$ originating from the bottom electrode (Fig. 8). The built-in electric fields were introduced following Eq. (7), with amplitudes varying from $E_0 = 0.1$ to 10 MV/cm. In Fig. 8, the electric field decay extends across a thickness of $\tau = 10$ nm. Results obtained with other values of τ are shown in Fig. S5 in the Supplemental Material [49].

In Fig. 8(a), a distinct shift in hysteresis is observed when employing a positive built-in field initiated from the bottom electrode. This shift effect manifests as a horizontal adjustment towards a positive applied electric field. Experimentally, to counterbalance this built-in field, an additional positive voltage bias at the top electrode becomes necessary, inducing the observed hysteresis shift. Notably, the magnitude of the shift is directly related to the built-in field amplitude. As its intensity increases, the hysteresis loop correspondingly shifts towards higher positive electric field values.

An opposite trend emerges in Fig. 8(b), when an identical but downward-oriented (towards the interface) field is considered. In this case, the hysteresis loop undergoes a shift towards negative electric field values. In addition, the simulations also

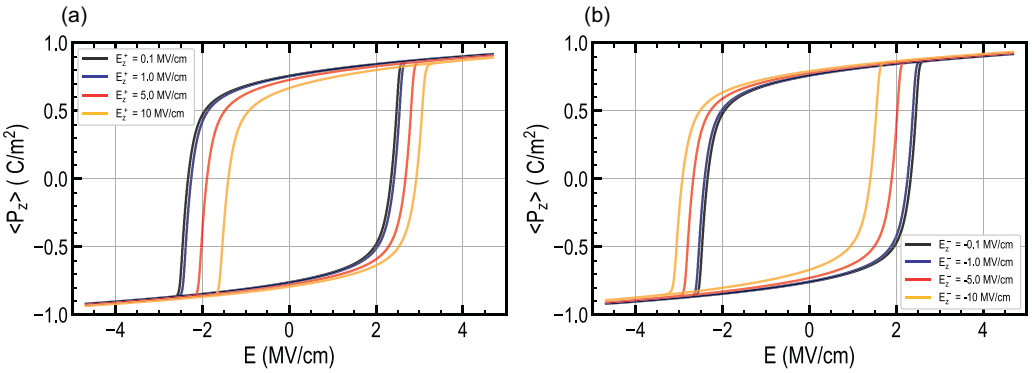

FIG. 8. Ferroelectric hysteresis loops obtained by phase-field simulations. A linearly decaying electric field $E_z^{\pm}$ starting from the bottom electrode is considered. Simulations include both (a) upward-oriented E_z^+ and (b) downward-oriented E_z^- fields, diminishing over a distance of 10 nanometers (see Fig. S4 in the Supplemental Material [49] for details). The amplitude of the additional electric field varies within the range of $E_0 = 0.1$ to 10 MV/cm.

show that as the built-in field extends from the interface, which would correspond to a larger width of the depletion region, the shift of the hysteresis loop increases (see, for instance, Figs. S4 and S5 in the Supplemental Material [49]).

V. SUMMARY AND CONCLUSIONS

The impact of oxygen vacancies on the polarization switching of a ferroelectric BFCO thin film grown on a Nb-STO substrate was investigated. A correlation between the oxygen vacancies, switching field values, and the imprint effect is found. By modifying the oxygen vacancy density through a series of heat treatments in reductive or oxidative environments, it is possible to reversibly change the switching fields. An uneven modification of the switching fields is demonstrated, with the largest change for the left-sided switching field which can be tuned between −1.00 and 1.09 V. The corresponding change of the mean imprint value is within the 1.2 and 2.2 V voltage interval. A mean imprint value of 1.9 V was found for the initial state of the film, i.e., before the annealing cycles. This confirms that the BFCO films are already V_O rich after synthesis, in agreement with the literature on other oxide thin films. Our results show a mean imprint increase, due to the shift effect, of up to 66% (with respect to the lowest measured imprint case), while the constrictive effect increases the width of the loops by about 121% (with respect to the narrowest measured loop). Note that the possibility to control the imprint by choosing the annealing conditions is appealing for various specific applications.

The experimental results obtained after annealing under H_2/Ar conditions clearly exhibit a shift of the hysteresis loops towards positive voltages. This shift originates from a directional built-in electric field lying in the space charge region of the Schottky contact between the BFCO film and the Nb:STO electrode. This built-in field also appears to be the most likely origin for the residual imprint. In addition, because oxygen vacancies can be considered as dopants, modifications of their density are expected to affect the built-in electric field through a modulation of the Fermi level. This dependence constitutes an interesting topic for future studies.

By considering oxygen vacancies as positively charged dopants [64], along with a built-in electric field at the bottom electrode interface, the simulations were able to qualitatively reproduce the hysteresis loop changes observed through PFM measurements. One could note that the combined constrictive and shift effects induced by the oxygen vacancies and the built-in electric field can be used to favor one polarization direction, an effect particularity significant when both coercive fields have the same sign. Our findings suggest that the upward or downward polarization direction can, respectively, be favored by engineering a *p*-type or *n*-type Schottky contact at the bottom electrode. These results highlight the central role played by the nature of the ferroelectric/electrode contact.

It can thus be concluded that oxygen vacancies, rather than just being detrimental to ferroelectric properties, can also be seen as an easy, accessible, and reversible way to tune the ferroelectric polarization properties, as is sometimes needed for devices.

Furthermore, our findings are also of relevance for gaining insights into the photovoltaic properties of BFCO material. As annealing under H_2/Ar conditions increases the oxygen vacancies density, which in turn induces a higher imprint, and a more uniform polarization direction is obtained. A more uniform intrinsic polarization direction is expected to provide better photovoltaic responses in ferroelectric-based solar cell applications through the generation of a directional depolarization electric field. Thus, the role of oxygen vacancies in the photovoltaic effect exhibited by these materials shall be considered in future photovoltaic studies. Our study can be of interest for controlling the switching field values of other supported oxide ferroelectric thin films.

ACKNOWLEDGMENTS

We thank N. Beyer for technical assistance. This work was supported by the French National Research Agency (ANR) Project QMat, No. 17-EURE-0024.

[1] D. Das, A. Barman, S. Kumar, A. K. Sinha, M. Gupta, R. Singhal, P. Johari, and A. Kanjilal, Synergistic effect of singly charged oxygen vacancies and ligand field for regulating transport properties of resistive switching memories, J. Phys. Chem. C **123**, 26812 (2019).

[2] M. G. Han, M. S. J. Marshall, L. Wu, M. A. Schofield, T. Aoki, R. Twesten, J. Hoffman, F. J. Walker, C. H. Ahn, and Y. Zhu, Interface-induced nonswitchable domains in ferroelectric thin films, Nat. Commun. **5**, 4693 (2014).

[3] L. Yin and W. Mi, Progress in $BiFeO_3$-based heterostructures: Materials, properties and applications, Nanoscale **12**, 477 (2020).

[4] S. Chatterjee, A. Barman, S. Barman, T. Chabri, S. Kar-Narayan, A. Datta, and D. Mukherjee, Role of oxygen vacancies on the low-temperature dielectric relaxor behavior in epitaxial $Ba_{0.85}Ca_{0.15}Ti_{0.9}Zr_{0.1}O_3$ thin films, Phys. Rev. Mater. **5**, 064415 (2021).

[5] H.-L. Zhou, Y.-P. Jiang, X.-G. Tang, Q.-X. Liu, W.-H. Li, and Z.-H. Tang, Excellent bidirectional adjustable multistage resistive switching memory in Bi_2FeCrO_6 thin film, ACS Appl. Mater. Interfaces **12**, 54168 (2020).

[6] M. Choi, A. Janotti, and C. G. Van de Walle, Native point defects in $LaAlO_3$: A hybrid functional study, Phys. Rev. B **88**, 214117 (2013).

[7] Y. M. Kim, A. Morozovska, E. Eliseev, M. P. Oxley, R. Mishra, S. M. Selbach, T. Grande, S. T. Pantelides, S. V. Kalinin, and A. Y. Borisevich, Direct observation of ferroelectric field effect and vacancy-controlled screening at the $BiFeO_3/La_xSr_{1-x}MnO_3$ interface, Nat. Mater. **13**, 1019 (2014).

[8] T. Yang, J. Wei, Z. Sun, Y. Li, Z. Liu, Y. Xu, G. Chen, T. Wang, H. Sun, and Z. Cheng, Design of oxygen vacancy in $BiFeO_3$-based films for higher photovoltaic performance, Appl. Surf. Sci. **575**, 151713 (2022).

[9] S. Hu, Z. Tang, L. Zhang, D. Yao, Z. Liu, S. Zeng, X. Guo, Y. Jiang, X.-G. Tang, L. Ma, Z. Nie, and J. Gao, Photo-induced negative differential resistance and carrier-transport mechanisms in Bi_2FeCrO_6 resistive switching memory devices, J. Mater. Chem. C **9**, 13755 (2021).

[10] X. G. Chen, X. B. Ma, Y. B. Yang, L. P. Chen, G. C. Xiong, G. J. Lian, Y. C. Yang, and J. B. Yang, Comprehensive study of the resistance switching in $SrTiO_3$ and Nb-doped $SrTiO_3$, Appl. Phys. Lett. **98**, 122102 (2011).

[11] U. Petralanda, M. Kruse, H. Simons, and T. Olsen, Oxygen vacancies nucleate charged domain Walls in ferroelectrics, Phys. Rev. Lett. **127**, 117601 (2021).

[12] M. Tyunina, J. Peräntie, T. Kocourek, S. Saukko, H. Jantunen, M. Jelinek, and A. Dejneka, Oxygen vacancy dipoles in strained epitaxial $BaTiO_3$ films, Phys. Rev. Res. **2**, 023056 (2020).

[13] H. Wang and K. Zeng, Characterization of domain structure and imprint of $Pb(Zn_{1/3}Nb_{2/3})O_3 - 4.5\%PbTiO_3$ (PZN-4.5%PT) single crystals by using PFM and SS-PFM techniques, Ceram. Intl. **46**, 4274 (2020).

[14] J. Lee, R. Ramesh, V. G. Keramidas, W. L. Warren, G. E. Pike, and J. T. Evans Jr., Imprint and oxygen deficiency in (Pb, La)(Zr, Ti)O_3 thin-film capacitors with La-Sr-Co-O electrodes, Appl. Phys. Lett. **66**, 1337 (1995).

[15] W. Sun, C. J. Bartel, E. Arca, S. R. Bauers, B. Matthews, B. Orvananos, B.-R. Chen, M. F. Toney, L. T. Schelhas, W. Tumas, J. Tate, A. Zakutayev, S. Lany, A. M. Holder, and G. Ceder, A map of the inorganic ternary metal nitrides, Nat. Mater. **18**, 732 (2019).

[16] R. W. Smaha, J. S. Mangum, I. A. Leahy, J. Calder, M. P. Hautzinger, C. P. Muzzillo, C. L. Perkins, K. R. Talley, S. Eley, P. Gorai, S. R. Bauers, and A. Zakutayev, Structural and optoelectronic properties of thin film $LaWN_3$, Phys. Rev. Mater. **7**, 084411 (2023).

[17] P. S. Brody, Large polarization-dependent photovoltages in ceramic $BaTiO_3$+ 5 wt.% $CaTiO_3$, Solid State Commun. **12**, 673 (1973).

[18] J. E. Spanier, V. M. Fridkin, A. M. Rappe, A. R. Akbashev, A. Polemi, Y. Qi, Z. Gu, S. M. Young, C. J. Hawley, D. Imbrenda, G. Xiao, A. L. Bennett-Jackson, and C. L. Johnson, Power conversion efficiency exceeding the Shockley-Queisser limit in a ferroelectric insulator, Nat. Photon. **10**, 611 (2016).

[19] S. Y. Yang, J. Seidel, S. J. Byrnes, P. Shafer, C.-H. Yang, M. D. Rossell, P. Yu, Y.-H. Chu, J. F. Scott, J. W. Ager, L. W. Martin, and R. Ramesh. Above-band-gap voltages from ferroelectric photovoltaic devices, Nat. Nanotechnol. **5**, 143 (2010).

[20] T. Choi, S. Lee, Y. J. Choi, V. Kiryukhin, and S.-W. Cheong, Switchable ferroelectric diode and photovoltaic effect in $BiFeO_3$, Science **324**, 63 (2009).

[21] X. Zhao, K. Song, H. Huang, W. Han, and Y. Yang, Ferroelectric materials for solar energy scavenging and photodetectors, Adv. Opt. Mater. **10**, 2101741 (2022).

[22] Y. Li, J. Fu, X. Mao, C. Chen, H. Liu, M. Gong, and H. Zeng, Enhanced bulk photovoltaic effect in two-dimensional ferroelectric $CuInP_2S_6$, Nat. Commun. **12**, 5896 (2021).

[23] Y. Yun, L. Muhlenbein, D. S. Knoche, A. Lotnyk, and A. Bhatnagar, Strongly enhanced and tunable photovoltaic effect in ferroelectric-paraelectric superlattices, Sci. Adv. **7**, eabe4206 (2021).

[24] R. Nechache, C. Harnagea, L. Cardenas, W. Huang, J. Chakrabartty, and F. Rosei, Bandgap tuning of multiferroic oxide solar cells, Nat. Photon. **9**, 61 (2015).

[25] Y. Yuan, Z. Xiao, B. Yang, and J. Huang, Arising applications of ferroelectric materials in photovoltaic devices, J. Mater. Chem. A **2**, 6027 (2014).

[26] R. Nechache, C. Harnagea, S. Licoccia, E. Traversa, A. Ruediger, A. Pignolet, and F. Rosei, Photovoltaic properties of Bi_2FeCrO_6 epitaxial thin films, Appl. Phys. Lett. **98**, 202902 (2011).

[27] F. Zheng, J. Xu, L. Fang, M. Shen, and X. Wu, Separation of the Schottky barrier and polarization effects on the photocurrent of Pt sandwiched $Pb(Zr_{0.20}Ti_{0.80})O_3$ films, Appl. Phys. Lett. **93**, 172101 (2008).

[28] B. R. Tak, M.-M. Yang, M. Alexe, and R. Singh, Deep-level traps responsible for persistent photocurrent in pulsed laser deposited beta-Ga_2O_3 thin films, Crystals **11**, 1046 (2021).

[29] H.-B. Zhang and M. Alexe, Optoelectronic functionality of $BiFeO_3SrTiO_3$ interface, Adv. Electr. Mater. **8**, 2100665 (2022).

[30] Y. Zhou, H.-K. Chan, C.-H. Lam, and F. Shin, Mechanisms of imprint effect on ferroelectric thin films, J. Appl. Phys. **98**, 024111 (2005).

[31] A. S. Borowiak, N. Baboux, D. Albertini, B. Vilquin, G. S. Girons, S. Pelloquin, and B. Gautier, Electromechanical response of amorphous $LaAlO_3$ thin film probed by scanning probe microscopies, Appl. Phys. Lett. **105**, 012906 (2014).

[32] G. E. Pike, W. L. Warren, D. Dimos, B. A. Tuttle, R. Ramesh, J. Lee, V. G. Keramidas, and J. T. Evans Jr., Voltage offsets in (Pb, La)(Zr, Ti)O_3 thin films, Appl. Phys. Lett. **66**, 484 (1995).

[33] Y. Jeong, V. Gaddam, Y. Goh, H. Shin, S. Lee, G. Kim, and S. Jeon, Oxygen vacancy control as a strategy to enhance imprinting effect in Hafnia ferroelectric devices, IEEE Trans. Electron Devices **70**, 354 (2023).

[34] K. Bao, J. Liao, F. Yan, S. Jia, B. Zeng, Q. Yang, M. Liao, and Y. Zhou, Enhanced endurance and imprint properties in $Hf_{0.5}Zr_{0.5}O_{2-\delta}$ ferroelectric capacitors by tailoring the oxygen vacancy, ACS Appl. Electron. Mater. **5**, 4615 (2023).

[35] Y. Noguchi, H. Matsuo, Y. Kitanaka, and M. Miyayama, Ferroelectrics with a controlled oxygen-vacancy distribution by design, Sci. Rep. **9**, 4225 (2019).

[36] H. Matsuo, Y. Kitanaka, R. Inoue, Y. Noguchi, and M. Miyayama, Switchable diode-effect mechanism in ferroelectric $BiFeO_3$ thin film capacitors, J. Appl. Phys. **118**, 114101 (2015).

[37] J. H. Lee, J. H. Jeon, C. Yoon, S. Lee, Y. S. Kim, T. J. Oh, Y. H. Kim, J. Park, T. K. Song, and B. H. Park, Intrinsic defect-mediated conduction and resistive switching in multiferroic $BiFeO_3$ thin films epitaxially grown on $SrRuO_3$ bottom electrodes, Appl. Phys. Lett. **108**, 112902 (2016).

[38] C. Ge *et al.*, Toward switchable photovoltaic effect via tailoring mobile oxygen vacancies in perovskite oxide films, ACS Appl. Mater. Interfaces **8**, 34590 (2016).

[39] A. Herklotz, S. F. Rus, C. Sohn, Santosh KC, V. R. Cooper, E.-J. Guo, and T. Z. Ward, Optical response of $BiFeO_3$ films subjected to uniaxial strain, Phys. Rev. Mater. **3**, 094410 (2019).

[40] G. Geneste, C. Paillard, and B. Dkhil, Polarons, vacancies, vacancy associations, and defect states in multiferroic $BiFeO_3$, Phys. Rev. B **99**, 024104 (2019).

[41] I. V. Maznichenko, S. Ostanin, L. V. Bekenov, V. N. Antonov, I. Mertig, and A. Ernst, Impact of oxygen doping and oxidation state of iron on the electronic and magnetic properties of $BaFeO_{3-\delta}$, Phys. Rev. B **93**, 024411 (2016).

[42] L. Zhang, Z. Wang, S. Shu, Y. Hu, C. Li, S. Ke, F. Li, and L. Shu, Origin of defects induced large flexoelectricity in ferroelectric ceramics, Phys. Rev. Mater. **6**, 094416 (2022).

[43] V. Sharma, G. Pilania, G. A. Rossetti, Jr., K. Slenes, and R. Ramprasad, Comprehensive examination of dopants and defects in $BaTiO_3$ from first principles, Phys. Rev. B **87**, 134109 (2013).

[44] H.-B. Zhang, M.-M. Yang, and M. Alexe, Boosting the photocurrent in $BiFeO_3$ thin films via a domain-wall-defect interaction, Adv. Photon. Res. **4**, 2200189 (2023).

[45] T. Yang, J. Wei, Y. Guo, Z. Lv, Z. Xu, and Z. Cheng, Manipulation of oxygen vacancy for high photovoltaic output in bismuth ferrite films, ACS Appl. Mater. Interfaces **11**, 23372 (2019).

[46] Y. Zhou, Y. K. Zhang, Q. Yang, J. Jiang, P. Fan, M. Liao, and Y. C. Zhou. The effects of oxygen vacancies on ferroelectric phase transition of HfO_2-based thin film from first-principle, Comput. Mater. Sci. **167**, 143 (2019).

[47] G. Wang, Y. Yang, D. Han, and Y. Li, Oxygen defective metal oxides for energy conversion and storage, Nano Today **13**, 23 (2017).

[48] S. Jesse, H. N. Lee, and S. V. Kalinin, Quantitative mapping of switching behavior in piezoresponse force microscopy, Rev. Sci. Instrum. **77**, 073702 (2006).

[49] See Supplemental Material at http://link.aps.org/supplemental/10.1103/PhysRevMaterials.8.054416 for additional experimental details and simulations parameters.

[50] E. G. Lee, D. J. Wouters, G. Willems, and H. E. Maes, Voltage shift and deformation in the hysteresis loop of Pb(Zr, Ti)O_3 thin film by defects, Appl. Phys. Lett. **69**, 1223 (1996).

[51] L. Baudry, Theoretical investigation of the influence of space charges on ferroelectric properties of $PbZrTiO_3$ thin film capacitor, J. Appl. Phys. **86**, 1096 (1999).

[52] T. Rojac, A. Bencan, B. Malic, G. Tutuncu, J. L. Jones, J. E. Daniels, and D. Damjanovic, $BiFeO_3$ ceramics: Processing, electrical, and electromechanical properties, J. Am. Ceram. Soc. **97**, 1993 (2014).

[53] K. Alhada-Lahbabi, D. Deleruyelle, and B. Gautier, Machine learning surrogate model for acceleration of ferroelectric phase-field modeling, ACS Appl. Electron. Mater. **5**, 3894 (2023).

[54] S. G. Casal, X. Bai, K. Alhada-Lahbabi, B. Canut, B. Vilquin, P. R. Romeo, S. Brottet, D. Albertini, D. Deleruyelle, M. Bugnet, I. C. Infante, and B. Gautier, Mechanical switching of ferroelectric domains in 33–200-nm-thick Sol-Gel-Grown $PbZr_{0.2}Ti_{0.8}O_3$ films assisted by nanocavities, Adv. Electron. Mater. **8**, 1 (2022).

[55] L.-Q. Chen, Phase-field models for microstructure evolution, Annu. Rev. Mater. Res. **32**, 113 (2002).

[56] Y. L. Li, S. Y. Hu, Z. K. Liu, and L. Q. Chen, Effect of substrate constraint on the stability and evolution of ferroelectric domain structures in thin films, Acta Mater. **50**, 395 (2002).

[57] K. Alhada-Lahbabi, D. Deleruyelle, and B. Gautier, Phase-field study of nanocavity-assisted mechanical switching in $PbTiO_3$ thin films, Adv. Electron. Mater. 2300744 (2024).

[58] Y. Cao, A. Morozovska, and S. V. Kalinin, Pressure-induced switching in ferroelectrics: Phase-field modeling, electrochemistry, flexoelectric effect, and bulk vacancy dynamics, Phys. Rev. B **96**, 184109 (2017).

[59] J. Wang, S. Q. Shi, L. Q. Chen, Y. Li, and T. Y. Zhang, Phase-field simulations of ferroelectric/ferroelastic polarization switching, Acta Mater. **52**, 749 (2004).

[60] J. J. Wang, X. Q. Ma, Q. Li, J. Britson, and L. Q. Chen, Phase transitions and domain structures of ferroelectric nanoparticles: Phase field model incorporating strong elastic and dielectric inhomogeneity, Acta Mater. **61**, 7591 (2013).

[61] V. V. Laguta, A. M. Slipenyuk, I. P. Bykov, M. D. Glinchuk, M. Maglione, D. Michau, J. Rosa, and L. Jastrabik, Electron spin resonance investigation of oxygen-vacancy-related defects in $BaTiO_3$ thin films, Appl. Phys. Lett. **87**, 022903 (2005).

[62] Y. Sharma, R. Martinez, R. Agarwal, D. Barrionuevo, R. K. Katiyar, A. Kumar, and R. S. Katiyar, Studies on structural, optical, magnetic, and resistive switching properties of doped $BiFe_{1-x}Cr_xO_3$ thin films, J. Appl. Phys. **120**, 194101 (2016).

[63] V. C. Lo, Modeling the role of oxygen vacancy on ferroelectric properties in thin films, J. Appl. Phys. **92**, 6778 (2002).

[64] P. Lutz, S. Moser, V. Jovic, Y. J. Chang, R. J. Koch, S. Ulstrup, J. S. Oh, L. Moreschini, S. Fatale, M. Grioni, C. Jozwiak, A. Bostwick, E. Rotenberg, H. Bentmann, and F. Reinert, Volatile two-dimensional electron gas in ultrathin $BaTiO_3$ films, Phys. Rev. Mater. **2**, 094411 (2018).